ELSEVIER

Journal of Alloys and Compounds 300–301 (2000) 242–253

Journal of ALLOYS AND COMPOUNDS

www.elsevier.com/locate/jallcom

Simple overlap model and crystal field analysis of Cs_2ZnCl_4:Co^{2+}. Correlation with optical and magnetic properties

J. Derouet[a,*], L. Beaury[a], P. Porcher[a], P.J. Deren[b]

[a]*Laboratoire de Chimie Appliquée de l'Etat Solide, ENSCP, 11 rue Pierre et Marie Curie, F-75231 Paris Cedex 05, France*

[b]*W. Trzebiatowski Institute of Low Temperature and Structure Research, Polish Academy of Sciences, ul. Okolna 2, P.O. Box 937, 50950 Wroclaw 2, Poland*

Abstract

The optical (energy level scheme) and magnetic properties (paramagnetic susceptibility as a function of temperature and g values) of Co^{2+} in a Cs_2ZnCl_4 single crystal were reproduced simultaneously according to the crystal field theory involving a set of free ions and B_q^k crystal field parameters. The Co^{2+} are placed in a weak tetrahedral ligand field. The crystal field parameters calculated from the structure are in good agreement with the experimental values. The correlation between the g values and B_q^k parameters is discussed.

Keywords: Overlap model; Optical properties; Magnetic properties; Crystal field simulation

1. Introduction

In a previous paper [1] we presented the experimental spectroscopic properties (absorption and emission spectra) of Cs_2ZnCl_4:Co^{2+}. The cobalt ions ($3d^7$) substitute for the zinc ions and are located in a pseudo-tetrahedral site.

The aim of this work was (i) to perform a semi-empirical calculation of the crystal field parameters (cfps) B_q^k from crystallographic data by the simple overlap model (SOM) and (ii) a simultaneous simulation of optical, paramagnetic and electronic paramagnetic resonance (EPR) data, by transfer of the computational techniques used for f^N configurations of the lanthanides [2]. In this latter case the absorption and emission transitions are numerous and well defined. The spectra are the experimental basis for an accurate simulation of the electronic structure and magnetic properties. Often, in addition to the classical electrostatic repulsion, spin–orbit coupling and crystal field interaction, two- and three-body interactions can be introduced together with other magnetic interactions. The description of the configuration is made on the $|SLJM\rangle$ basis. The computed properties depend on parameters which can be freely varied in the hamiltonian. The number of cfps B_q^k depends on the symmetry at the crystallographic site.

The $|SM_SLM_L\rangle$ basis is usually considered for the 3d electrons of the transition metals together with the ligand field parameter $10Dq$, which is the separation between the two types of d orbitals d_γ and d_ε. The orbitals d_γ (d_{z^2} and $d_{x^2}-d_{y^2}$) and d_ε (d_{xy}, d_{xz}, d_{yz}) are also denoted e and t_2 according to their associated irreducible representations in the T_d point group. The spin–orbit coupling has generally been neglected in the calculations or considered as a second-order perturbation [3,4].

The difference with the rare earths lies in the fact that the 3d orbitals are more affected by the character of the ligands, leading to the observation of large absorption or emission bands as well as to a stronger electron–phonon coupling [5]. The simulation process differs in the case of d elements because the absorption and emission spectra yield only a few crystal field levels and the optical data can hardly be considered alone. We must then take into account the paramagnetic susceptibility as a function of the temperature and the EPR data.

2. Experimental background

The Cs_2ZnCl_4 crystal was synthesized and grown by the method described in Ref. [1]. The unit cell of Cs_2ZnCl_4 is orthorhombic and belongs to the *Pnam*-D_{2h}^{16} space group with four formula units for the unit cell. Cs_2CoCl_4 and Cs_2CuCl_4 are isostructural to Cs_2ZnCl_4. It was found that the cell parameters are $a = 0.976$ nm, $b = 0.740$ nm and

*Corresponding author.

0925-8388/00/$ – see front matter
PII: S0925-8388(99)00778-1

$c = 1.298$ nm. Puget et al. [6] showed that the structure is constructed on the basis of slightly distorted $ZnCl_4$ tetrahedra. They pointed out the fact that, in the crystal unit, there are two Cs ions, the first surrounded by 11 halogen ions, which make a tight and anisotropic cage, while the second has only nine neighbours and therefore is less tight than the first. Co^{2+} replace Zn^{2+} and occupy a single crystallographic site with C_s point symmetry (close to D_{2d}). The two C_s sites are structurally equivalent. One site is deduced from the other by a rotation of 41.52° around the *b*-axis [7]. This makes them non-equivalent from a magnetic point of view.

The absorption spectrum was recorded from a crystal mounted in an Oxford (Model 1204) continuous flow helium cryostat on a Cary 5 spectrophotometer. The crystal was oriented and the polarizers used were from the Cary equipment. The emission spectrum was recorded on a Cerny–Turner type monochromator equipped with a R406 Hamamatsu photomultiplier. The crystal was excited with an ILA 120 argon laser from Carl Zeiss Jena [1].

The paramagnetic susceptibility measurements were performed using a DSM8 susceptometer from 4.2 to 300 K in a magnetic field of 1.1 T. The setup was calibrated with $BaFe_{12}O_{19}$ as the standard. The diamagnetic correction was calculated using the values (in units of 10^{-6} emu mol^{-1}) of -37, -18 and -23 for Cs^+, Co^{2+} and Cl^-, respectively [8].

The polycrystalline powder EPR spectrum of Cs_2ZnCl_4 doped with 10% Co^{2+} has been recorded at 18 K using a Bruker ER220D spectrometer with 100 kHz modulation. The principal *g* values for the ground state level have been found to be anisotropic with $g_1 = 2.3$, $g_2 = 3.9$ and $g_3 = 4.7$. They are comparable to those found for low-symmetry pseudo-tetrahedral high-spin cobalt(II) complexes [9,10].

3. Theoretical background

3.1. The simple overlap model

The simple overlap model (SOM) developed by Malta [11,12] has been applied successfully to reproduce the phenomenological cfps for a great number of lanthanides as well as for some 3d element compounds [13–16]. In this model, the cfps are calculated from the atomic positions in the structure.

According to the SOM, the crystal field effect can be calculated by assuming a potential produced by an effective charge distribution over a small region, proportional to the overlap between 4f and ligand wavefunctions, situated around the mid point of the metal–ligand distance. The B_q^k parameters are written as

$$B_q^k = \rho\left(\frac{2}{1 \pm \rho}\right)^{k+1} A_q^k \langle r^k \rangle$$

where A_q^k is the lattice sum of neighbours belonging to the first coordination sphere associated with an effective charge, $\langle r^k \rangle$ are the radial integrals (for cobalt, $\langle r^2 \rangle$ and $\langle r^4 \rangle$ are equal to 1.2587 (a.u.)^2 and 3.706 (a.u.)^4, respectively [17]), and ρ is the overlap between the 3d orbitals of the central ion and the s and p orbitals of the ligand, the value of which varies as a function of the metal–ligand distance, *R*, according to the power law $\rho = \rho_0(R_0/R)^{3.5}$ [18], R_0 being the shortest metal–ligand distance.

The $\pm$ sign characterizes the displacement of the charge barycenter from the metal–ligand mid-distance; the minus sign is applied when $r_{\text{metal}} < r_{\text{ligand}}$ [12,19]. If we consider that the 3d orbitals are expanded due to penetrating ligand orbitals and that 3d–4s mixing may be very important, it is not unrealistic to consider ρ values between 0.10 and 0.30. The overlap integrals are larger for the 3d elements than for the lanthanides, for which ρ lies between 0.05 and 0.08 [14,20].

The simple overlap model, in which an aspect of the chemical bonding is taken into account, may be regarded as a starting point to carry out practical crystal field calculations. The determined B_q^k are introduced for the diagonalization of the secular determinant of the $3d^7$ configuration. It is also useful to introduce the total ligand crystal field strength parameter δ [21], which permits a comparison of the effect of different ligands:

$$\delta = \left[\frac{1}{n}\sum_k \sum_{q=-k}^{q=+k} \frac{1}{2k+1}(B_q^k)^2\right]^{1/2}$$

with $n = 2$ and $k = 2, 4$ for d elements.

3.2. Crystal-field calculations

The description of an electronic configuration is based on the central field model. The electrons are initially assumed to move independently from each other in an effective central field and are then submitted to various independent interactions. Their effects are represented by non-zero matrix elements between the $|\text{SLJM}\rangle$ states of the configuration. The quantitative effect of the interaction is usually described according to the Racah algebra techniques. This method, almost completely described by Wybourne [22], has been used extensively for a realistic simulation of the nf^N configurations of rare earth and actinide ions [23]. The hamiltonian including the different interactions can be written as

$$H_{\text{TOT}} = H_0 + H_{\text{CR}} + H_{\text{CF}} + H_{\text{SO}}$$

— H_0 is the spherically symmetric one-electron part of the free-ion hamiltonian which separates the ground configuration from the excited configurations.

— H_{CR} represents the coulombic repulsion characterized by the Slater integrals F^k (or the Racah parameters *B* and *C*); it also includes the two-body interaction (Trees parameter α).

— H_{CF} is the crystal-field hamiltonian which consists of

the sum of products between the crystal-field parameters (cfps) and the spherical harmonics C_q^k:

$$H_{CF} = \sum_{k=0}^{4}\sum_{q=0}^{k} B_q^k[C_q^k + (-1)^q C_{-q}^k] + iS_q^k[C_q^k - (-1)^q C_{-q}^k]$$

In the above expression, B_q^k and S_q^k represent the real and imaginary parts of the cfps. The number of non-zero parameters depends on the crystallographic point site symmetry. k is even inside a given configuration.

Simulation of the $3d^N$ configurations frequently requires the use of the descending symmetry procedure, starting from cubic symmetry (in this case $|B_4^4/B_0^4| = 0.5976$) which involves only the crystal field parameter Dq, directly related to B_0^4 by $B_0^4 = 21Dq$ (for quaternary symmetry).

As indicated above, the symmetry of the point site is low, C_s, slightly distorted from T_d. Thus, we introduce the descending symmetry procedure $T_d \rightarrow D_{2d} \rightarrow C_{2v} \rightarrow C_s$. The latter symmetry lowering induces imaginary parts for the cfps. It is not taken into account because it leads to too many cfps. Finally, the symmetry considered is C_{2v} for which the hamiltonian is written as

$$H_{C_{2v}} = B_0^2C_0^2 + B_2^2(C_2^2 - C_{-2}^2) + B_0^4C_0^4 + B_2^4(C_2^4 - C_{-2}^4) + B_4^4(C_4^4 - C_{-4}^4)$$

According to the slight distortion from T_d, B_0^2 is expected to be small and B_2^2 and B_2^4 very small, whereas B_4^4/B_0^4 is close to the cubic ratio.

— H_{SO} is the spin–orbit interaction characterized by the spin–orbit coupling constant ζ ($\lambda = \pm\zeta/2S$) [3].

In this approach the differences between the $3d^N$ and $4f^N$ (or $5f^N$) configurations lie in: (i) the number of parameters introduced by the H_{CR} and H_{CF} interactions, and (ii) the order of magnitude of these interactions. For the 3d elements, the crystal field strength can be an order of magnitude greater than for the 4f elements, whereas H_{CR} is of the same order of magnitude and H_{SO} smaller, which explains why the $|SM_SLM_L\rangle$ basis can often replace the $|SLJM\rangle$ basis to facilitate the calculations. The $3d^7$ configuration of Co^{2+} involves 120 $|SLJM\rangle$ kets. Due to the odd number of electrons the number of levels is reduced to 60 Kramers doublets in the absence of a magnetic field.

The wavefunctions derived from the diagonalization of the secular determinant are used to calculate the paramagnetic susceptibility and its variation versus temperature according to the van Vleck formula [24] and the magnetic splitting factors g.

4. Application to Co^{2+} in Cs_2ZnCl_4 (pseudo-tetrahedral site)

4.1. Spectroscopic data

Ferguson has shown [25] that the group of peaks observed in the absorption spectra of Co^{2+} in Cs_2ZnCl_4 can be described in C_S symmetry using the T_d notation. Considered as a three hole case, Co^{2+} ($3d^7$) in a tetrahedral crystal field has the same energy level scheme as an octahedral d^3 ion, except for a change in the sign of λ and in the relation $V_{tetra} = -4/9V_{octa}$ between the crystal field potentials. These configurations split into two terms of multiplicity four, ^4P and ^4F (ground state), which show large half-width band transitions due to the strong crystal field interaction, and six terms of multiplicity two (^2G, ^2P, ^2H, $^2D1$, $^2D2$, ^2F), which depend weakly on the crystal field strength.

The d^7 configuration spans a series of multiplets, such as

$$^4F \Rightarrow {}^4A_2 + {}^4T_2 + {}^4T_1$$

$$^4P \Rightarrow {}^4T_1$$

$$^2G \Rightarrow {}^2E + {}^2T_1 + {}^2A_1 + {}^2T_2$$

The ground state, the quartet $^4A_2$ (^4F), is orbitally non-degenerate.

The whole absorption spectrum is shown in Fig. 1. The first excited level, labelled $^4T_2$, is not observed here since it lies out of the range of our spectrophotometer. This transition, forbidden in T_d symmetry, can be observed for a distorted site, although with low intensity.

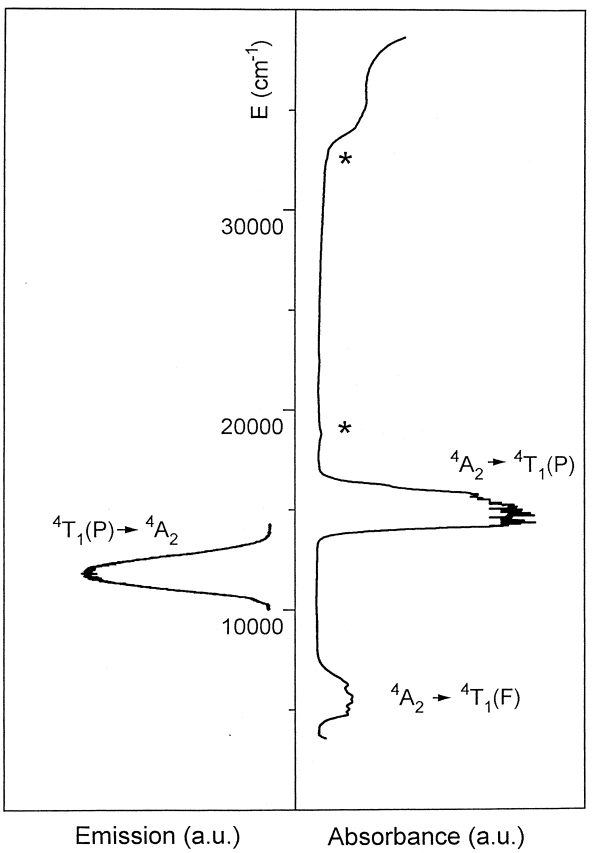

Fig. 1. Comparison between absorption and emission spectra. The spin-forbidden transitions of weak intensity are situated in the region between the two asterisks (*).

Table 1
Experimental and calculated energy levels $^4T_1$ (^4F) (cm^{-1})

Abs. zero-phonon	$\rho = 0.12$	% ^4F	Set A	% ^4F	$\rho = 0.13$	% ^4F	Set B	% ^4F
4852	4943	97.8	4892	99.8				
5061	5187	97.4	5134	99.9				
5263	5346	98.2	5208	99.8				
5616	5599	97.6	5446	99.9	5654	97.0	5705	96.4
					5874	96.4	5921	95.4
6042	6149	97.4	6092	99.8	6072	97.7	6086	99.0
6231	6184	97.3	6180	99.8	6301	97.0	6292	97.5
					6936	96.5	6894	94.1
					6969	96.4	6974	93.9

- Two transitions are allowed for Co^{2+} in tetrahedral symmetry:
  (i) $^4A_2 \rightarrow {}^4T_1(^4F)$ from 4700 to 7000 cm^{-1} reveals six main peaks (Table 1, column 1) and additional peaks due to the vibrational modes.
  (ii) $^4A_2 \rightarrow {}^4T_1(^4P)$ is the strongest band in the absorption spectrum observed from 12 500 to 17 000 cm^{-1}. This spin-allowed transition is broadened by phonons and strongly mixed with the $^4A_2 \rightarrow {}^2E + {}^2T_1(^2G)$ transition (Table 2, column 1).
- The peaks from 16 500 to 35 000 cm^{-1} represent transitions from $^4A_2$ to the levels of the ^2G, ^2H, ^2P, $^2D_2$ and ^2F terms, i.e. 35 Kramers doublets (Tables 2 and 3). These spin-forbidden transitions become allowed by spin–orbit coupling. They are expected to be of weak intensity.

A large $^4T_1(^4P) \rightarrow {}^4A_2$ emission band centred at 11 800 cm^{-1} was found [1]. It is also shown in Fig. 1. The half-width of this band is about 2000 cm^{-1}.

The additional absorption peaks correspond to the vibrational modes of the matrix Cs_2ZnCl_4. Although Cs_2ZnCl_4 and Cs_2CoCl_4 are isomorphous, some lines could be attributed to specific modes of the $[CoCl_4]^{2-}$

Table 2
Experimental and calculated energy levels $^4T_1$ (^4P) and $^2E + {}^2T_1$ (^2G) (cm^{-1}) with the percentage of multiplicity 2 and 4 for $Cs_2ZnCl_4:Co^{2+}$. The first column presents the observed experimental lines (1 to 11). These values minus the shift due to phonons are shown in the second column (1b to 11b). The lines attributed to ^2G (observed experimental absorption without shift due to the phonons) could be the lines 3, 5, 6 for $\rho = 0.12$ and 3, 4, 6, 7 for $\rho = 0.13$. The lines attributed to ^4P (with a shift of -1700 cm^{-1}) could be 4b, 7b, 8b for $\rho = 0.12$ and 7b, 9b, 10b, 11b for $\rho = 0.13$

Exp (absorption)	Exp -1700 cm^{-1}	$\rho = 0.12$	^{2S+1}L	% of $2S+1=2$	% of $2S+1=4$	$\rho = 0.13$	^{2S+1}L	% of $2S+1=2$	% of $2S+1=4$
	(1b) 12 623								
	(2b) 12 800								
	(3b) 13 227								
	(4b) 13 757	*(4b)* 13 717	^4P	0.6	99.4				
		13 730	^4P	0.9	99.1				
	(5b) 13 900								
	(6b) 14 039	*(6b)* 14 073	^4P	0.5	99.5				
	(7b) 14 250	*(7b)* 14 158	^4P	2.4	97.6	*(7b)* 14 308	^4P	1.3	98.7
						14 318	^4P	1.1	98.9
(1) 14 323		14 347	^4P	3.6	96.4				
(2) 14 500	*(8b)* 14 522	*(8b)* 14 520	^4P	2.0	98.0				
	(9b) 14 632					*(9b)* 14 712	^4P	1.4	98.6
	(10b) 14 845					*(10b)* 14 780	^4P	5.3	94.7
	(11b) 14 863					*(11b)* 14 950	^4P	18.2	81.8
(3) 14 927		*(3)* 14 969	^2G	99.1	0.9	*(3)* 14 950	Mix	18.2	81.8
		15 044	^2G	99.3	0.7	15 072	^2G	87.6	12.4
						15 115	Mix	41.6	58.4
						15 153	^2G	67.4	32.6
(4) 15 457		15 255	^2G	98.6	1.4	*(4)* 15 389	^2G	88.0	12.0
(5) 15 600		*(5)* 15 676	^2G	98.2	1.8				
(6) 15 739		*(6)* 15 781	^2G	98.5	1.5	*(6)* 15 795	^2G	95.6	4.4
(7) 15 950						*(7)* 15 914	^2G	96.8	3.2
(8) 16 222									
(9) 16 332									
(10) 16 545									
(11) 16 563									

Table 3
Comparison of the calculated doublet energy levels for the optical fit Set B and the overlap $\rho = 0.13$. The non-observed lines are *in italic*[a]

Exp. abs. ⊥	Exp. abs. ∥	$\rho = 0.13$	$\Delta/(\perp+\parallel)/2$	Main compon.		Set B	$\Delta/(\perp+\parallel)/2$	Main compon.	
				$^{2S+1}$L	%			$^{2S+1}$L	%
17 304	17 300	17 320	18	^{2}G	78.5	17 149	−155	^{2}G	82.5
17 458	17 473								
17 635	17 645	17 692	52	^{2}G	56.0	17 609	−31	^{2}G	77.7
17 769									
17 807		17 877	70	^{2}G	50.4				
18 042	18 048	18 252	206	^{2}G	72.4	18 127	83	^{2}G	85.5
	18 473								
18 608									
18 890	18 890					18 863	−27	^{2}H	34.8
19 222	19 243								
19 460	19 452	19 480	24	^{2}H	36.8	19 452	−4	^{2}H	41.4
19 696									
	19 925	19 851	−74	^{2}P	31.2	19 890	−35	^{2}P	34.3
		20 038	–	^{2}H	48.9				
20 235	20 215	20 150	−75	^{2}H	40.5	20 222	−3	^{2}H	58.9
		20 443	–	^{2}H	34.8				
20 595		20 517	−78	^{2}H	57.7	20 560	−35	^{2}P	23.7
20 880						20 724	−156	^{2}H	46.5
21 230						21 134	−96	^{2}H	19.8
21 280		21 468	188	^{2}D2	32.4	21 495	215	^{2}H	34.1
21 848		21 805	−43	^{2}H	35.2				
21 872									
21 928	21 928								
21 955	21 955					21 955	0	^{2}P	38.2
22 063	22 068								
22 200	22 208	22 189	−15	^{2}H	16.8	22 146	−58	^{2}D2	29.9
	22 273	22 287	14	^{2}P	25.4				
22 429	22 429	22 513	84	^{2}H	32.5				
						22 774	–	^{2}H	51.2
22 936	22 936					22 903	−33	^{2}H	67.0
23 230	23 224	23 354	127	^{2}H	77.6				
		23 851	–	^{2}H	55.5	*23 805*	–	^{2}H	40.1
		23 954	–	^{2}H	57.6				
24 103	24 103	24 192	89	^{2}H	51.0	23 866	−237	^{2}H	25.6
						24 349	–	^{2}H	49.5
24 483	24 483	24 520	37	^{2}D2	34.3	24 498	15	^{2}H	40.3
24 566	24 576	24 558	−13	^{2}D2	34.8				
24 662						24 695	33	^{2}D2	40.4
26 372		26 498	126	^{2}D2	26.6	26 082	−290	^{2}D2	40.8
26 673		26 562	−111	^{2}D2	23.5	26 719	46	^{2}D2	32.8
30 606	30 606								
30 817		30 936	119	^{2}F	86.4				
						31 016	–	^{2}F	80.5
						31 102	–	^{2}F	83.0
31 192	31 192	31 225	33	^{2}F	80.8	31 183	−9	^{2}F	91.9
		31 303	–	^{2}F	90.4				
		31 562	–	^{2}F	92.5				
		32 386	–	^{2}F	88.8	*31 715*	–	^{2}F	95.0
32 456	32 456	32 487	31	^{2}F	81.0	32 406	−50	^{2}F	95.2
						32 527	–	^{2}F	84.9
32 690	32 690	32 593	−97	^{2}F	86.5	32 602	−88	^{2}F	93.7

[a] $\Delta/(\perp+\parallel)/2$ is the deviation between the calculated energy levels and the average experimental values.

entity. These latter are known for $[CoCl_4]^{2-}$ salts [26], and we have not redetermined their positions.

The IR and Raman spectra of Cs_2ZnCl_4 were studied by Lamba et al. [27] and they found for the strongest vibrational mode due to Zn–Cl stretch $\nu_1(A_1) = 288\ cm^{-1}$. We have found this mode in the absorption spectrum with a value of 283 cm^{-1}. The other modes, $\nu_2(E) \approx 116\ cm^{-1}$, $\nu_4(F_2) \approx 130\ cm^{-1}$ and $\nu_3(F_2) \approx 298\ cm^{-1}$, which are difficult to determine, are present but with weak intensity [1].

4.2. Effect of the vibrating lattice environment on optical properties

Because the electronic and lattice systems are coupled together, the initial and final states for the electronic transitions are electron-plus-lattice states. Consequently, the observed optical electronic transitions present a dual electronic/vibrational character. Fig. 2 presents the single configurational model in which the electronic ground and excited energy states are represented by parabolae. Horizontal lines in a parabola represent discrete vibronic levels.

We consider two general situations:

- The excited state potential surface may have the same equilibrium nuclear distance Q_0 as the ground state: $^4A_2$ ($d_\varepsilon^3\, d_\gamma^4$). This is the case for the first level ^2E which has the same configuration $d_\varepsilon^3\, d_\gamma^4$. For these transitions, sharp lines not enlarged by the phonons are expected.
- For the levels owing to different configurations, the minima are shifted relative to one another. This is the case, for example, of the spin-allowed transition $^4A_2(d_\varepsilon^3\, d_\gamma^4) \Leftrightarrow {}^4T_1(d_\varepsilon^5\, d_\gamma^2)$. The width and the shape of the absorption and emission bands depend on the configurational coordinate displacement Q. The energy E_d defined in Fig. 2 is a measure of the difference in coupling and is equal to half the Stokes shift. It is written as [28]

$$E_d = S\hbar\omega$$

The Huang–Rhys parameter S [29] is a dimensionless constant which parametrizes the difference in coupling between the initial and final states of the transition. $\hbar\omega$ is the energy of the strongest phonon of the considered host material (in our case, $\hbar\omega = 283$ cm^{-1} [1]).

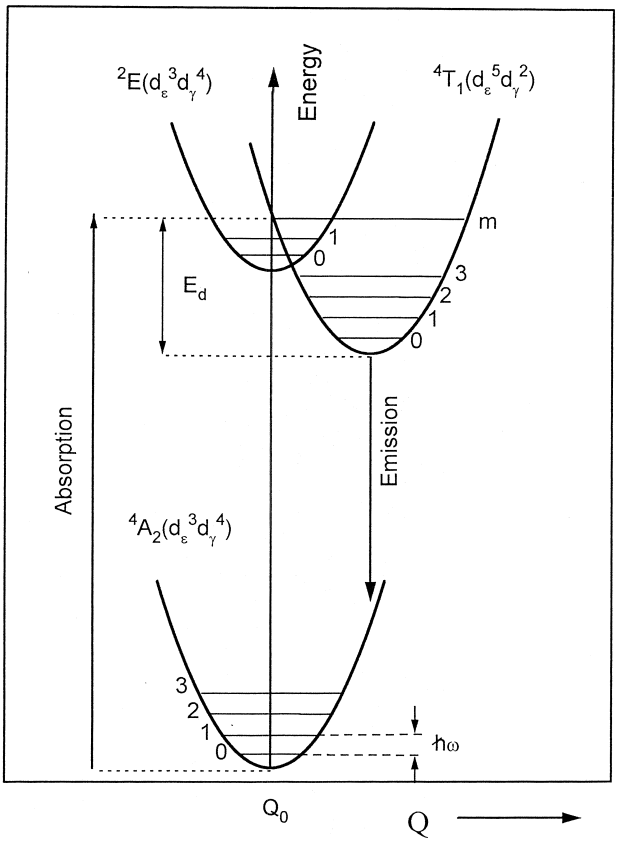

Fig. 2. Configurational coordinate diagram in the harmonic approximation for three electronic states (E_d is the half Stokes shift). Horizontal lines in a parabola represent discrete vibronic levels.

By comparing the absorption and emission spectra of the transition $^4A_2 \leftrightarrow {}^4T_1(^4P)$ we evaluate the Stokes shift to be 3400 cm^{-1}. To estimate the positions of the potential minima of the levels, we assume that all quartet levels could be described by the same parabola with the same Stokes shift, consequently $E_d \cong 1700$ cm^{-1} and the Huang–Rhys parameter S is close to 6.

On the other hand, according to the Franck–Condon principle [30], the mean nuclear positions remain unchanged during the transitions of the electrons. Therefore, a transition between two levels with different equilibrium distance involves the creation of m phonons, which depends on the coupling to the crystal lattice. The zero-phonon transitions involve two states of the same configuration. The half-width Γ_0 (at 0 K) [31] of a transition can be estimated by the following formula:

$$\Gamma_0 = m\hbar\omega = 2\hbar\omega(2S)^{1/2}$$

By assuming $\Gamma_{10\ K} \approx \Gamma_0$ for the large emission band $^4T_1(^4P) \rightarrow {}^4A_2$, the estimated S for the quartet level is also close to 6.

Although the levels coming from the ^2H, ^2P, and ^2D terms have configurations different from the ground level (i.e. $d_\varepsilon^3\, d_\gamma^4$ and $d_\varepsilon^5\, d_\gamma^2$), the bands remain relatively narrow: $\Gamma_0 \approx \Gamma_{10\ K} \approx 270$ cm^{-1} (Fig. 4 in Ref. [1]). This implies $S \approx 0.1$ and we can conclude that the Stokes shift ($\approx$60 cm^{-1}) is almost negligible in this case.

4.3. Results and discussion

4.3.1. SOM calculation

Initially, SOM calculations were performed in the overlap domain 0.10–0.30. The cobalt–chloride bonding is assumed to be relatively ionic with an effective charge factor $g_{Cl} = -1$ equal to its nominal value. The B_q^k parameters obtained from the calculation are introduced for the diagonalization of the secular determinant. The complete energy level scheme of Co^{2+} (zero-phonon lines) calculated with $\rho = 0.12$ and $\rho = 0.13$ gives the best agreement with the experimental scheme (Fig. 3). Nevertheless, an irregular shift (600–1000 cm^{-1}) is observed between these two schemes. The determined parameters (F^2, F^4, α, ζ and cfps B_q^k) are given in Table 4.

For the $^4A_2 \rightarrow {}^4T_1(^4F)$ transition (4700–7000 cm^{-1}), the

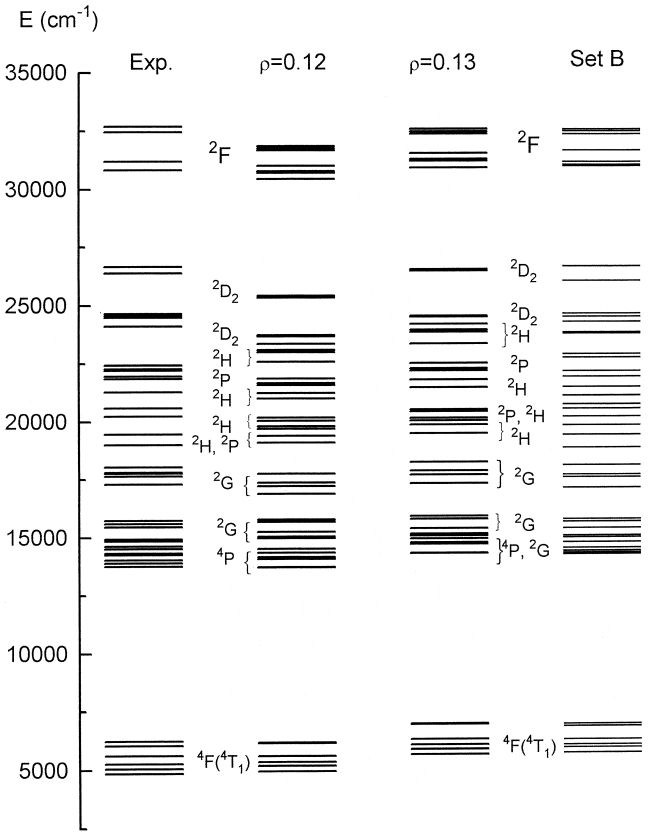

Fig. 3. Experimental energy level scheme compared with computed values from: (i) SOM calculation for the overlaps $\rho = 0.12$ and $\rho = 0.13$; and (ii) optical adjustment (Set B). The equivalence between the free-ion and crystal field notations is listed in the text.

observed absorption lines are relatively narrow and the zero-phonon lines can be estimated. The SOM calculation gives better results for $\rho = 0.12$ (Table 1).

For the term of multiplicity four $^4T_1(^4P)$, the zero-phonon lines are not determined, but the Stokes shift is estimated to be 3400 cm^{-1}. This does not allow a complete assignment of the experimental data for the broad absorption band 12 500–17 000 cm^{-1} (partially resolved at 12 K). Consequently, we propose two different assignments in correlation with $\rho = 0.12$ and 0.13 (Table 2). The Dq/B ratio is equal to 0.42 and 0.48 for $\rho = 0.12$ and 0.13 (Table 4). According to the Tanabe–Sugano diagram [3], where the crossover between $^2E(^2G)$ and $^4T_1(^4P)$ appears for $Dq/B \cong 0.5$, we are in a situation of weak crystal field strength confirmed by the relatively small δ values (Table 4). δ is also smaller than for the isostructural Cs_2CuCl_4 ($\delta = 4072$ cm^{-1}) or for $Co_{0.5}Ti_2(PO_4)_3$ ($\delta = 5240$ cm^{-1}) [16]; to compare these crystal field strength parameters with those defined by Auzel [21] we have to multiply them by the factor $(4\pi)^{1/2}$.

In both cases, $^2E(^2G)$ is calculated with higher energy than $^4T_1(^4P)$. However, for $\rho = 0.13$, more important mixing is noted between the group of nominal states $^2E(^2G)$ and $^2T_1(^2G)$ with $^4T_1(^4P)$. As an example, the wavefunctions associated with one component with the label ''^4P'' are

for $\rho = 0.12$ (at 14 347 cm^{-1}): 96.4% $|^4P\rangle$ + 1.6% $|^2F\rangle$ + 2.0% $|^2P,D,G,H\rangle$

for $\rho = 0.13$ (at 15 515 cm^{-1}): 56.8% $|^4P\rangle$ + 1.6% $|^4F\rangle$ + 29.1% $|^2G\rangle$ + 12.5% $|^2P,D,H\rangle$

which underlines the impossibility of characterizing an energy level with only a single $|SLJM\rangle$ ket.

Fig. 4 shows a Tanabe–Sugano-like diagram (also including the splitting due to the spin–orbit coupling and to a non-cubic crystal field) for a limited range of Dq/B. More precisely, great mixing is found between the energy levels in the $0.45 \leq Dq/B \leq 0.57$ range. This makes almost impossible a precise attribution of the energy levels deduced by deconvolution of the broad experimental absorption spectrum. Depending on the value of ρ, the energy of the lowest zero-phonon line is calculated at 13 717 cm^{-1} ($\rho = 0.12$) or at 14 308 ($\rho = 0.13$). The other calculated lines are also shifted, and for each overlap only six or seven lines can be attributed (Table 2).

Although the relative positions of the ^4P and ^2G levels remain uncertain, the experimental decay time of the broad emission band, measured at liquid helium temperature, is very short (50 ns) [1]. This permits us to assume that the emission from the lowest level is spin allowed and that the ^4P could consequently be assumed to be located at a lower energy than the ^2G. This situation is best reproduced for $\rho = 0.12$.

The situation is more simple in the case of the spin-forbidden transitions ($^4A_2 \rightarrow {}^2P$, $^2D_{1,2}$, ^2F, ^2G, ^2H) because the Stokes shift is small (≈ 60 cm^{-1}) and there is no overlap between levels of different multiplicities. Experimental and calculated energies can be directly compared. $\rho = 0.13$ and $\rho = 0.12$ induce an irregular shift of the energy level scheme (for example, 1000 cm^{-1} for $^2D_2$ and 330 cm^{-1} for the ^2G terms) (Fig. 3). $\rho = 0.13$ gives the best simulation (Table 3).

4.3.2. Phenomenological simulation

The aim of the present simulation is to consider the optical and magnetic data simultaneously and to reproduce these data by using a set of phenomenological parameters. The number of levels is not sufficient to perform the adjustment with the exact C_s point symmetry of Co^{2+}. The calculation is then carried out with the C_{2v} symmetry. The involved parameters consist of four free-ion (F^2, F^4, α and ζ) and five real crystal field parameters (B_0^2, B_2^2, B_0^4, B_2^4 and B_4^4).

The energy level sequence is used as a conducting scheme for the simulation, whereas the paramagnetic susceptibility and its variation as a function of temperature

Table 4
Parameters (cm^{-1}) and g values

	Exp.	Optical fit			SOM calculation			
		Set A	Set B[a]		$\rho = 0.12$		$\rho = 0.13$	
g_{Cl}					−1	−1[a]	−1	−1[a]
F^2		60 172	58 506	58 506	58 696	58 696	58 790	58 790
F^4		46 538	43 646	43 646	44 488	44 488	44 720	44 720
α		28.04	36.51	36.51	28.47	28.47	25.06	25.06
ζ		[410][b]	[410]	[410]	410	410	410	410
B_0^2		−2641	−2833	−2833	−759	−759	−850	−850
B_1^2					269	269	302	302
B_2^2		[−10]	355	*−60*	281	*40*	313	*40*
B_0^4	−6825	−6006	−7105	−7105	−6102	−6102	−6997	−6997
B_1^4					−185	−185	−212	−212
B_2^4		−1045	−1028	−1028	−770	−770	−885	−885
B_3^4					−539	−539	−617	−617
B_4^4	4079	4293	4828	4828	4198	4198	4814	4814
B_2^2/B_0^2		−0.004	−0.125	*0.021*	−0.37	*−0.053*	−0.37	*−0.047*
B_2^4/B_0^4		0.174	0.145	0.145	0.126	0.126	0.126	0.126
B_4^4/B_0^4	Cub	−0.71	−0.68	−0.68	−0.69	−0.69	−0.69	−0.69
δ		2207	2518		2029		2352	
Rms		106	90					
Lev. nb		14	27					
B	728	700	699	699	693	693	693	693
C	3349	3693	3464	3464	3531	3531	3549	3549
C/B	4.6	5.2	4.96	4.96	5.1	5.1	5.12	5.12
Dq	325	286	338	338	291	291	333	333
Dq/B	0.45	0.408	0.484	0.484	0.42	0.42	0.481	0.481
g_1	2.3	2.28	1.48	2.25	2.01	2.50	1.95	2.47
g_2	3.9	4.27	1.93	4.22	2.33	4.16	2.14	3.94
g_3	4.7	5.09	6.49	4.96	6.33	5.05	6.28	5.09

[a] For Set B, $\rho = 0.12$ and $\rho = 0.13$, the second column is obtained by replacing B_2^2 by the values which give the best agreement for g factors.
[b] The parameters in brackets are fixed.

as well as the g magnetic splitting factors provide the most important data.

In a first step, we determine only one free-ion parameter (B) and one crystal field parameter (B_0^4 or Dq) from spin-allowed transitions [1]. Then the spin–orbit coupling constant is fixed at 410 cm^{-1} corresponding to a reduced free-ion value [32] and the other free-ion parameter C is related to B by the hydrogenic ratio $C \cong 4B$ [33]. For the adjustment, we take two starting points based on the known zero-phonon lines:

(i) Only $^4A_2$, $^4T_1(^4F)$, $^2D_2$ and ^2F are introduced. The B_2^2 cfp is fixed to a small value ($\cong 10$ cm^{-1}), sufficient to lift the degeneracy, and we obtain Set A.
(ii) $^4A_2$, $^4T_1(^4F)$ and all the well-defined spin-forbidden transitions. This adjustment leads to Set B (Table 4).

Note that the values of B_0^4 and B_4^4 for Sets A and B are in accordance with those corresponding to $\rho = 0.12$ and 0.13, respectively.

4.4. Paramagnetic susceptibility

The paramagnetic susceptibility is calculated according to the van Vleck formula [2,24]; the used wavefunctions are derived from the simulations described above. This calculation is carried out taking into account the whole configuration. The calculated and experimental average values are reported in Fig. 5, which presents the temperature dependence of the reciprocal magnetic susceptibility of the $Cs_2ZnCl_4:Co^{2+}$ sample. The variation of the susceptibility is slightly different for the two overlaps $\rho = 0.12$ and $\rho = 0.13$. The curves are comparable to those deduced from the optical fit A and B, respectively. We have retained $\rho = 0.13$ which gives a curve closer to the experimental one. The agreement between calculated and experimental values is fairly good at low temperature. There is a deviation above 100 K. This deviation may be associated with the evolution of the crystal field parameters with temperature, related to a possible variation of the central atom–ligand distances [34].

At this stage of the discussion, it is impossible to choose one set of parameters. It is not unrealistic to estimate $0.12 < \rho < 0.13$ and to consider $285 < Dq < 340$ cm^{-1}. However, the g values calculated by the adjustment to the optical data (Set B) as well as by the semi-empirical method are in disagreement with the experiment. A systematic analysis of these g values as a function of the wavefunction composition for the ground state needs to be performed.

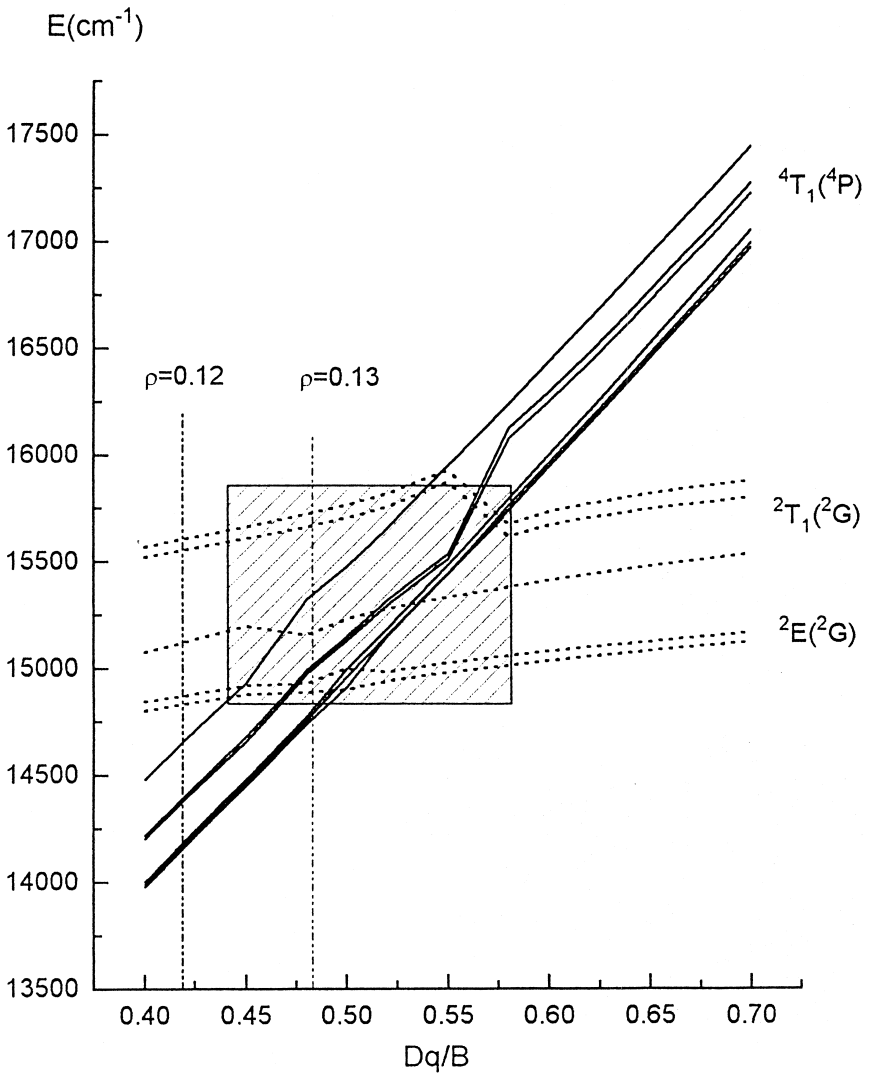

Fig. 4. Tanabe–Sugano-like diagram of the $^4T_1(^4P)$ with regard to the $^2T_1$, $^2E(^2G)$ levels as a function of the Dq/B ratio for a weak field situation (calculations were carried out for $|B_4^4/B_0^4| = 0.69$, the value determined by SOM, the other parameters being equal to zero).

4.5. g values

The g values are very sensitive to a slight distortion in the coordination environment of the metal ion and the anisotropy calculation of the g factor depends on the ground state wavefunction composition [2,35]. Although a single crystallographic site is present, there are two non-equivalent molecules per unit cell since the principal g_1, g_2, and g_3 do not correspond to the molecular g_x, g_y and g_z factors. However, we can consider that the three experimental values, determined on a powder sample, are representative of the crystallographic site of Co^{2+}, with a C_s point site symmetry. We can compare them directly with the calculated values, from the phenomenological simulation or from SOM. In this last case, although an overlap of 0.12 is relatively satisfying, a systematic analysis of the variation of the g values is attempted.

In a first step, Fig. 6a presents the variation of the g values when the $|B_4^4/B_0^4|$ ratio is distorted from the cubic ratio. In that case, B_0^4 corresponds to its SOM calculated value ($B_0^4 = -6102$ cm^{-1} for $\rho = 0.12$), the other cfps being set to zero, the distortion assumed to be axial. The intersection between the two curves $g_\parallel$ and $g_\perp$ is obtained when the $|B_4^4/B_0^4|$ ratio has the cubic value (0.5976) and the best agreement between experimental and calculated values is found for $|B_4^4/B_0^4| \geq 0.62$. The experimental values $|g_1| = 2.3$, $|g_2| = 3.9$ and $|g_3| = 4.7$ can be compared to the calculated $g_\parallel$ and $g_\perp$. It can be assumed that $g_\parallel$ can be taken as g_1, and $g_\perp$ as $[(g_2^2 + g_3^2)/2]^{1/2}$. The vertical dashed line represents the ratio value (0.69) determined by SOM. This is close to the value obtained when the crystal field parameters vary freely in the phenomenological simulation of the energy level scheme (Table 4).

If we now consider the variation of g as a function of $|B_4^4/B_0^4|$, but with all distortion parameters (i.e. also including B_0^2, B_2^2 and B_2^4 cfps) fixed to their values determined for $\rho = 0.12$ (Table 4), it is impossible to

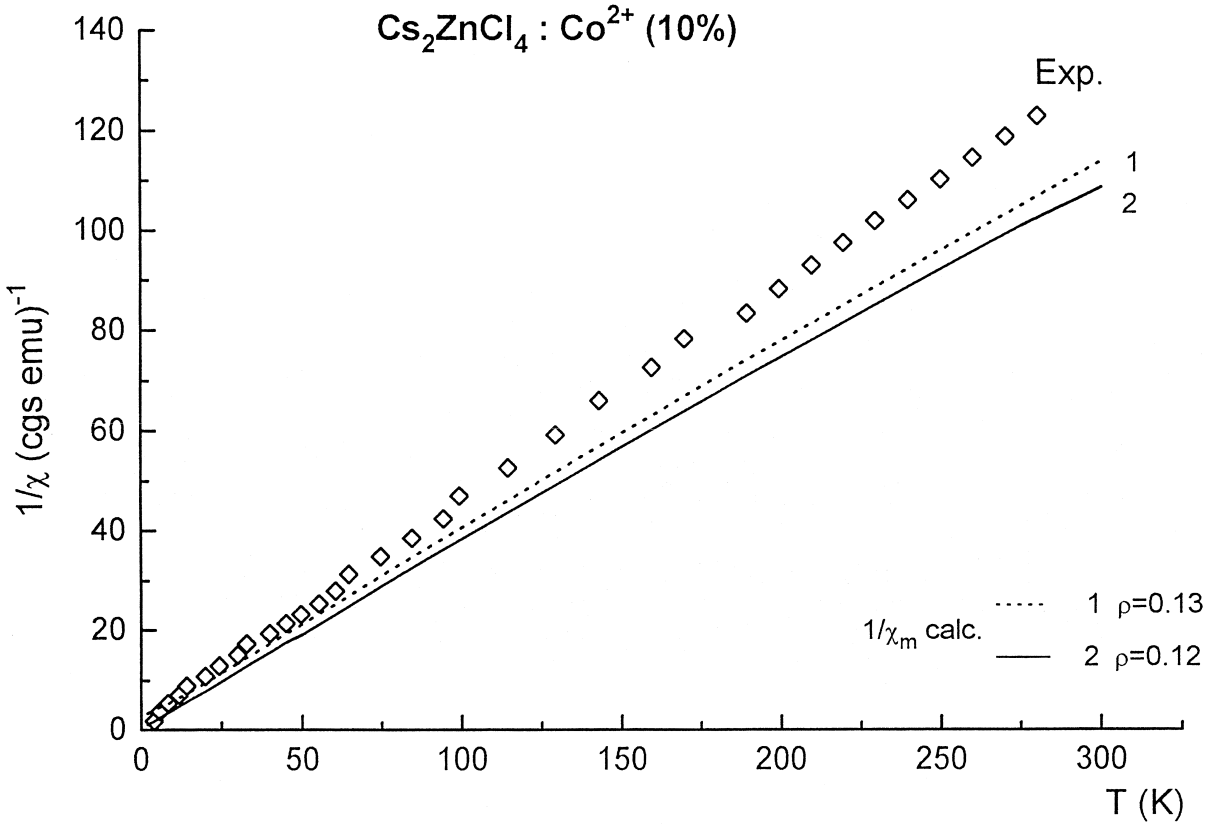

Fig. 5. Experimental and calculated inverse paramagnetic susceptibility versus temperature (calculations carried out for $\rho = 0.12$ and $\rho = 0.13$).

obtain agreement between experimental and calculated g values. The most sensitive variation is due to B_2^2, for which small variations induce strong modifications in the g anisotropy. Fig. 6b shows this important sensitivity. We can then determine a probable region for which B_2^2 gives good agreement between experimental and calculated g values. The B_2^2 fluctuation can be estimated in the 25–55 cm^{-1} range (hatched region). These positive values are in agreement with the sign determined by SOM. However, a narrow negative domain of B_2^2 is also estimated to reproduce the g anisotropy. In both cases, the $|B_2^2|$ value remains weak; this has already been observed for divalent copper in tetragonal or pseudo-tetragonal symmetries [36,37]. At this point, the total energy level scheme and the paramagnetic susceptibility do not depend on this distortion.

The g values of the lowest Kramers doublets are determined by the relative weight of the low symmetry crystal field components and spin–orbit coupling. In several cases the major distortions of the g values are attributed to the interactions with the ions of the second coordination sphere [38]. In the SOM model, only the nearest ions are considered, and the long distance electrostatic effects are not included. This consideration could be one of the reasons for the discrepancy for the cfps of rank 2.

4.6. Zero-field splitting (ZFS)

We also point out that the splitting between the two lowest Kramers doublets of high-spin Co^{2+} depends on the crystal field strength, the relative magnitude of the distortion from cubic symmetry and of the spin–orbit coupling strength (Table 4). Consequently, the experimental zero-field splitting (ZFS), defined classically by parameter $2D$ in units of energy, is a good indication of the distortion with regard to the binary axes. The parameters of rank 4 are those determined for $\rho = 0.12$ and are considered as exact. For Cs_2ZnCl_4:Co^{2+}, the experimental $2D$ parameter is 9 cm^{-1}, determined from specific heat measurements [39]. This value localizes B_0^2 between -3000 and -2000 cm^{-1}. For the overlap the calculated B_0^2 is -759 cm^{-1} and $2D$ is equal to 6.8 cm^{-1}. Good agreement is found for the phenomenological parameter Set A ($B_0^2 = -2641$ cm^{-1} and $2D = 8.8$ cm^{-1}) and for Set B ($B_0^2 = -2833$ cm^{-1} and $2D = 9.3$ cm^{-1}).

5. Conclusion

The present study underlines that the process of the simultaneous simulation of spectroscopic and magnetic

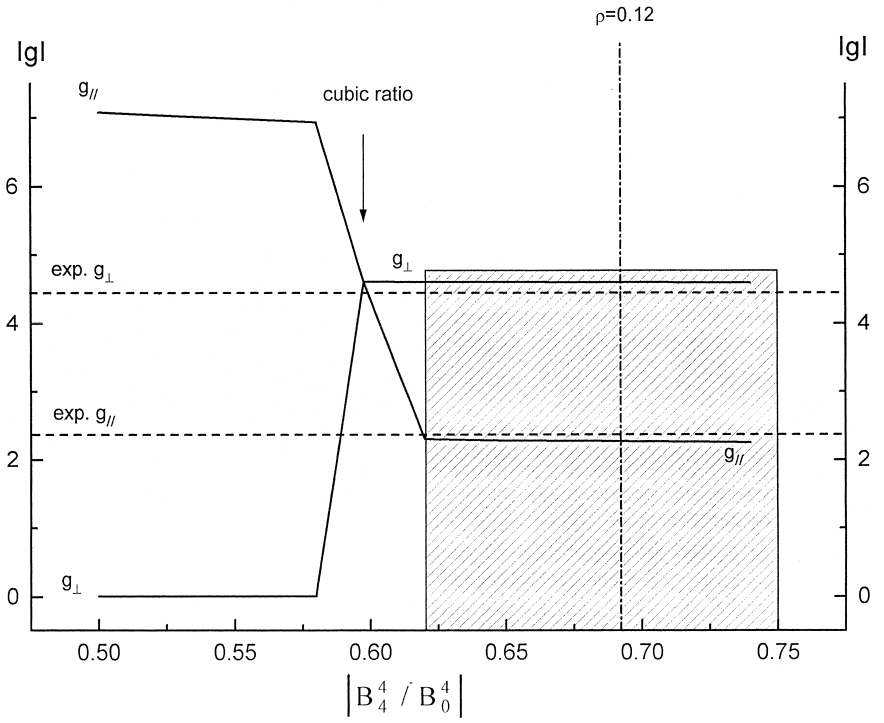

(a)

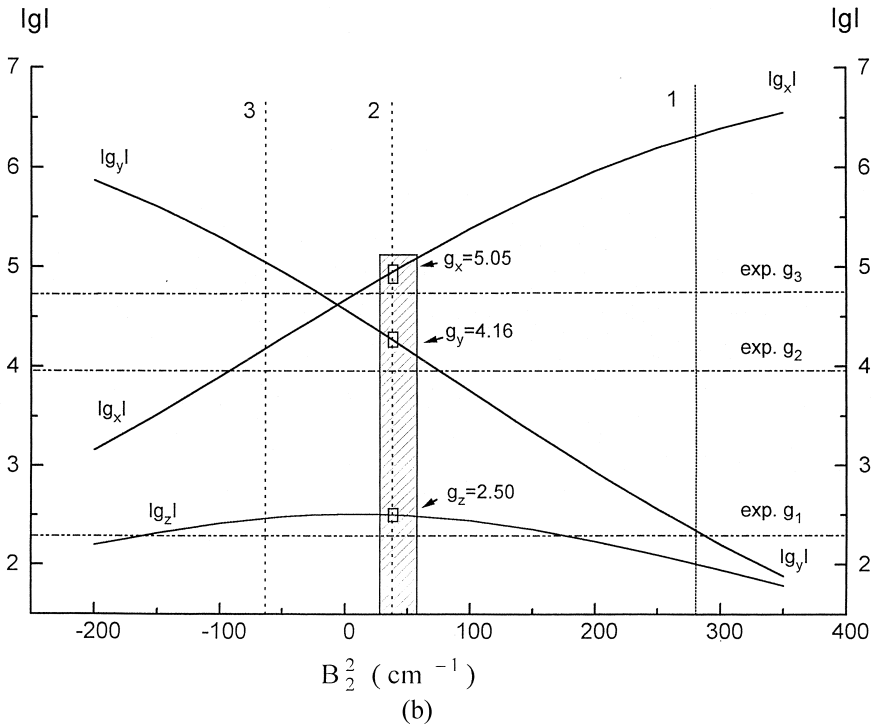

(b)

Fig. 6. (a) Calculated $|g|$ factors versus the $|B_4^4/B_0^4|$ ratio. B_0^4 is fixed to its value for $\rho = 0.12$ and the other cfps are zero. (b) Influence of the B_2^2 crystal field parameter on the $|g|$ factors. All the other parameters determined for $\rho = 0.12$ are fixed. The vertical lines correspond to the following particular values: (1) $B_2^2 = 281\ cm^{-1}$ determined by SOM; (2) $B_2^2 = 40\ cm^{-1}$, the best estimation from SOM (see Table 4); (3) $B_2^2 = -60\ cm^{-1}$, the best estimation from Set B (see Table 4).

properties of a 3d ion constitutes a good description of the electron configuration based on the one center model in spite of an important overlap between the metal 3d–ligand orbitals and of the vibronic coupling. In the present case, the study of several properties leads us to reproduce them with a good approximation (about 10%) for divalent cobalt in the Cs_2ZnCl_4 matrix.

The B_q^k parameters were calculated from the SOM model and compared with those deduced from the optical absorption spectrum, perturbed by vibronic transitions. In both cases, the calculation takes into account all the states of the d^7 configuration and relates the whole energy level scheme to the paramagnetic susceptibility. The g values were also calculated, but only from the ground state wavefunction. They are closely associated with the zero-field splitting value which is dependent on the coordination geometry [40]. The difficulty lies in the fact that a property can be represented against the evolution of the parameters as a number associated with a point in multidimensional space.

From the SOM calculations various possible sets of parameters were obtained as a function of the overlap ρ and the effective charge g_{Cl}. These are estimated with respect to consideration of the bonding strength. An overlap value of $\rho = 0.12–0.13$ and an effective charge equal to the nominal charge for chloride ($g_{Cl} = -1.0$) gave good results.

Comparing with the phenomenological values, a good correlation is found for the fourth-order cfps parameters. On the contrary, the second rank cfps are poorly estimated, which permits us to envisage different hypotheses:

(i) the effect of the second coordination sphere (or even longer distance effects) on the calculated cfps;
(ii) the hypersensitivity related to the ground state wavefunction composition. The latter is strongly dependent on the features of the lowest energy levels (ZFS and g EPR). A study of irregular or monotonous zones in tridimensional space g, B_0^2, B_2^2 could be an indication either of an amplification mechanism of the structural disorder in a narrow crystal-field domain, or of a very slow evolution of this disorder.
(iii) the influence of the phonons on the d^N configuration must not be neglected. Better knowledge of the different phonons involved could modify the nature of the wavefunction composition.

Acknowledgements

The authors thank D. Svoronos for providing the samples and D. Simons for measuring the g factors.

References

[1] J. Deren, J. Derouet, D. Svoronos, P. Porcher, J. Mol. Struct. 404 (1997) 167.
[2] L. Beaury, J. Derouet, M. Escorne, P. Porcher, J. Phys.: Condensed Matter 6 (1994) 5169.
[3] B.N. Figgis, Introduction to Ligand Fields, Interscience, New York, 1966.
[4] S. Sugano, Y. Tanabe, H. Kanimura, Multiplets of Transition Metal Ions in Crystal, Academic Press, New York, 1970.
[5] S.M. Uba, J.M. Baranowski, Phys. Rev. B 17 (1978) 69.
[6] R. Puget, M. Jannin, R. Perret, L. Godefroy, Ferroelectrics 107 (1990) 229.
[7] S. Bailleul, Thesis, Paris, 1990.
[8] L.N. Mulay, Magnetic Susceptibility, Wiley, New York, 1963.
[9] A. Bencini, C. Benelli, D. Gatteschi, C. Zanchini, Inorg. Chem. 18 (8) (1979) 2137.
[10] H. Drulis, K. Dyrek, K.P. Hoffmann, S.K. Hoffmann, A. Weselucha-Birczynska, Inorg. Chem. 24 (1958) 4009.
[11] O.L. Malta, Chem. Phys. Lett. 87 (1982) 27.
[12] O.L. Malta, Chem. Phys. Lett. 88 (1982) 353.
[13] O.L. Malta, G.F. De Sa, Quim. Nova (Brazil) 6 (1983) 123.
[14] O.L. Malta, S.L.J. Ribeiro, M. Faucher, P. Porcher, J. Phys. Chem. Solids 52 (1991) 587.
[15] J. Derouet, L. Beaury, P. Porcher, R. Olazcuaga, J.M. Dance, G. Leflem, M. El Bouari, A. El Jazouli, J. Solid State Chem. (in press).
[16] P. Porcher, M. Couto Dos Santos, O.L. Malta, Phys. Chem. Chem. Phys 1 (1999) 397.
[17] S. Fraga, J. Karkowski, K.M.S. Saxena, Handbook of Atomic Data, Elsevier, Amsterdam, 1976.
[18] C.K. Jorgensen, Modern Aspects of Ligand Field Theory, North-Holland, Amsterdam, 1971.
[19] G.P. Barnett, M.C. Pires Costa, R. Ferreira, Chem. Phys. Lett. 25 (1974) 49.
[20] G. Burns, J. Chem. Phys. 42 (1965) 377.
[21] F. Auzel, O. Malta, J. Phys. 44 (1983) 201.
[22] B.G. Wybourne, Spectroscopic Properties of Rare Earths Ions, Interscience, New York, 1965.
[23] W.T. Carnall, G.L. Goodmann, K. Rajnak, R.S. Rana, A systematic analysis of the lanthanides doped into a single crystal of LaF_3, Argonne National Laboratory Report, USA, 1988.
[24] J.H. Van Vleck, J. Appl. Phys. 39 (1968) 365.
[25] J. Ferguson, J. Chem. Phys. 36 (1963) 116.
[26] K.W. Hipps, U. Mazur, J. Phys. Chem. 91 (1987) 5218.
[27] O.P. Lamba, S.K. Sinha, Solid State Commun. 57 (5) (1986) 365.
[28] B. Di Bartolo, G. Armagan, Spectroscopy of Solid State Laser-Type Materials, Plenum Press, New York, 1987.
[29] K. Huang, A. Rhys, Proc. R. Soc. (London) A 204 (1950) 406.
[30] E.U. Condon, Phys. Rev. 32 (1928) 858.
[31] B. Henderson, G.F. Himbusch, Optical Spectroscopy of Inorganic Solids, Clarendon Press, Oxford, 1989.
[32] E. König, S. Kremer, Ber. Bunsenges. 78 (8) (1974) 786.
[33] E. König, Struct. Bond. (Berlin) 9 (1971) 175.
[34] L. Beaury, G. Calvarin, J. Derouet, J. Hölsä, E. Säilynoja, J. Alloys Comp. 275–277 (1998) 646.
[35] P. Caro, J. Derouet, M. Belkhiria, M. Benamara, M. Dasbabi, J.M. Dance, G. Leflem, J. Chim. Phys. (Paris) 91 (1994) 293.
[36] S. Bailleul, P. Porcher, J. Mol. Phys. 66 (1989) 605.
[37] S. Bailleul, J. Hölsä, P. Porcher, Eur. J. Solid State Inorg. Chem. 31 (1994) 431.
[38] A. Edgar, J. Phys. C 9 (1976) 4303.
[39] M.V. Makinen, L.C. Kuo, M.B. Yim, G.B. Wells, J.M. Fukuyama, J.E. Kim, J. Am. Chem. Soc. 107 (1985) 5245.
[40] J.N. McElearney, S. Merchant, G.E. Shankle, R.L. Carlin, J. Chem. Phys. 66 (1977) 450.